Modelling of stress field during Submerged Arc Weld surfacing taking into account heat of the weld and phase transformation effect

J. Winczek [1,*], K. Makles[1], M. Gucwa[1], R. Gnatowska[1] and M. Hatala[2]

[1] Faculty of Mechanical Engineering and Computer Science, Czestochowa University of Technology, 42-201 Czestochowa, Poland
[2] Faculty of Manufacturing Technologies, Technical University of Kosice with a seat in Prešov, 080 01 Prešov, Slovakia

Abstract

In work the model of stress calculation and analysis of stress field during single-pass SAW (Submerged Arc Welding) surfacing have been presented. In temperature field solution the temperature changes caused by the heat of weld and by electric arc have been taken into consideration. Kinetics of phase changes during heating is limited by temperature values at the beginning and at the end of austenitic transformation, while progress of phase transformations during cooling has been determined on the basis of time-temperature-transformation (TTT) - welding diagram. The stress state of thermal loaded flat has bean described assuming planar section hypothesis and simple Hooke's law and using integral equations of stress equilibrium. Dependence of stresses on strains is assumed on the basis of tensile curves of particular structures, taking into account the influence of temperature. The analysis of stress state has been presented for SAW surfacing S355 steel plate.

1. Introduction

Modelling of thermomechanical states in the surfacing or rebuilding by welding, requires the determination of temperature field. It is necessary to calculate the shares of structural elements taking into account their changes that occur as a result of phase transformations. Finally the thermal and structural strains enable the determination of temporary and residual stresses.

2. Temperature field

In modelling of temperature field during welding dominate two approaches: analytical [1 - 7] and numerical [8 - 16], looking for a solution for particular welding methods and types of joints. In analytical description of the temperature

---

*Corresponding author. Email: winczek@gmail.com

field, the bimodal heat source model has been used [17]. This model assumes physically one heat source – an electric arc, and the heat transfer to the surfaced object is divided into the heat transferred directly through the electric arc and through molten detached and transferred to the forming weld. Then the temperature field is represented by formula:

$$T(x,y,z,t)-T_0 = T_a(x,y,z,t)+T_w(x,y,z,t). \quad (1)$$

where: $T_a(x,y,z,t)$ and $T_w(x,y,z,t)$ are temperature fields caused respectively by the heat of direct impact of an electric arc and by the heat of the weld reinforcement (consumed to melt the electrode), T_0 – initial temperature of material.

Then the geometry of the weld is presented in Fig. 1, where h_w is the height of the weld (weld reinforcement – the part of the weld above the surface of the surfaced material), d_p is the depth of material thickness loss (e.g. depth of wear zone), and Δl results from considering the volume of material supplied from the electrode. Analytical description of the temperature field caused by the direct impact of the electric arc with Gaussian heat distribution (Fig. 2) is shown in [18], whereas considering the heat stored in the liquid metal imposed on the surface is presented in [19].
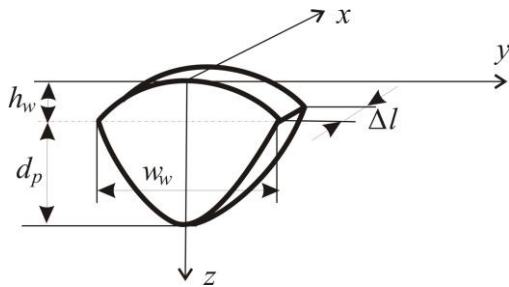

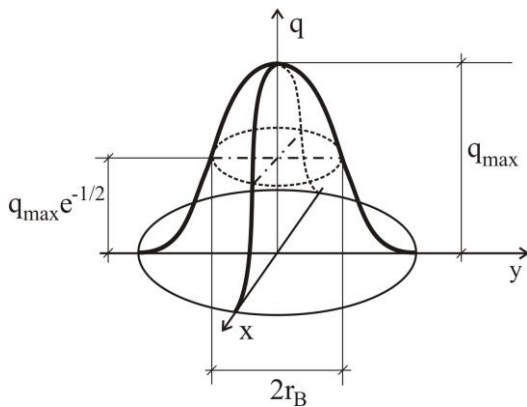**Figure 1.** Geometry of the weld

Figure 2. Gaussian distribution of heat source

For accepted scheme of the single-pass surfacing (Fig. 3), the temperature field (1) is defined as follows:

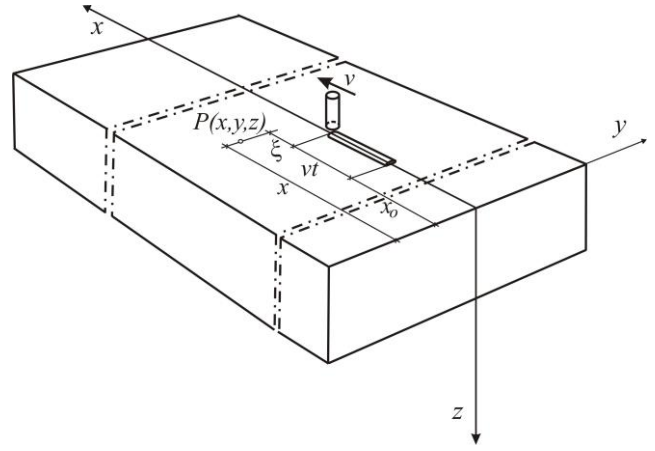- for time $t \leq t_c$, where t_c is the total time of making of the weld:

Figure 3. Arc weld surfacing scheme

- for time $t \leq t_c$, where t_c is the total time of making of the weld:

$$T(x,y,z,z_0,t)-T_0 =$$
$$= A_w \int_0^t \{H_H(t'')(F_2(y,z)+F_3(y,z)-F_4(y,z)-F_1(y,z))\}dt'' + \quad (2)$$
$$+ A_H \int_0^t F_H(t'')dt''$$

- for time $t > t_c$:

$$T(x,y,z,z_0,t)-T_0 =$$
$$= A_w \int_0^{t_c} \{H_C(t')(G_2(y,z)+G_3(y,z)-G_4(y,z)-G_1(y,z))\} + \quad (3)$$
$$+ A_C \int_0^{t_c} F_C(t')dt'$$

where:

$$A_H = \frac{3\dot{q}}{16C_p\rho(\pi a)^{1.5}z_0}exp\left(-\frac{\xi v}{2a}-\frac{v^2 t_0}{4a}\right) \quad (4)$$

$$A_w = \dot{q}_v / 8C_p\rho\sqrt{\pi a} \quad (5)$$

$$A_C = 3\dot{q}/(16C_p\rho\pi a z_0) \quad (6)$$

$$H_H(t'')=\frac{1}{\sqrt{t''}}\left(\left(erf\left(\frac{\Delta l - 2(\xi + vt'')}{4\sqrt{at''}}\right)+\right.\right.$$
$$\left.\left.+ erf\left(\frac{\Delta l + 2(\xi + vt'')}{4\sqrt{at''}}\right)\right)\right) \quad (7)$$

$$F_H(t'') = \frac{1}{t''+t_0} exp\left(-\frac{\xi^2}{4a(t''+t_0)} - \frac{v^2 t''}{4a}\right)$$

$$\left\{\left(1 - \frac{z^2 + 2at''}{z_0^2}\right)\right.$$

$$\left(\left(erf\left(\frac{z+z_0}{2(at'')^{0,5}} - \Phi(z)erf\left(\Phi(z)(z)\frac{z-z_0}{2(at'')^{0,5}}\right)\right)\right) + \right. \tag{8}$$

$$+ \frac{4at''}{z_0^2}\left(\frac{z+z_0}{(4\pi at'')^{0,5}} exp\left(-\frac{(z-z_0)^2}{4at''}\right) + \right.$$

$$\left.\left.- \frac{z-z_0}{(4\pi at'')^{0,5}} exp\left(-\frac{(z+z_0)^2}{4at''}\right)\right)\right)\right\}$$

$$H_C(t') = \frac{1}{\sqrt{(t-t')}}\left(erf\left(\frac{\Delta l - 2(x-vt'-x_0)}{4\sqrt{a(t-t')}}\right) + \right. \tag{9}$$

$$\left. + erf\left(\frac{\Delta l + 2(x-vt'-x_0)}{4\sqrt{a(t-t')}}\right)\right)$$

$$F_C(t') = \frac{1}{t+t_0-t'}$$

$$exp\left(-\frac{(x-vt'-x_0)^2 + (y-y_0)^2}{4a(t+t_0-t')}\right)$$

$$\left\{\left(1 - \frac{z^2 + 2a(t-t')}{z_0^2}\right)\left(erf\left(\frac{z+z_0}{2(a(t-t'))^{0,5}}\right) + \right.\right. \tag{10}$$

$$\left. - \Phi(z)erf\left(\Phi(z)\frac{z-z_0}{2(a(t-t'))^{0,5}}\right)\right) +$$

$$\frac{4a(t-t')}{z_0^2}\left(\frac{z+z_0}{(4\pi a(t-t'))^{0,5}} exp\left(-\frac{(z-z_0)^2}{4a(t-t')}\right) + \right.$$

$$\left.\left.- \frac{z-z_0}{(4\pi a(t-t'))^{0,5}} exp\left(-\frac{(z+z_0)^2}{4a(t-t')}\right)\right)\right\}$$

$$\xi = x - v(t+t_0) - x \tag{11}$$

$$\Phi(z) = \begin{cases} -1 & dla \ z \in \langle 0, z_0 \rangle \\ 1 & dla \ z \in (z_0, \infty) \end{cases} \tag{12}$$

$$t_c = l/v \tag{13}$$

a - thermal diffusivity [m²/s], C_p - specific heat [J/kgK], ρ - density [/kg m], x_0 [m] and l [m] m are the coordinates of the start and length of the weld respectively. Quantity t_0 / s characterizes surface heat source distribution whereas $r_B^2 = 4at_0$ [20] (compare Figure 2). Functions $G_1 - G_4$ and $F_1 - F_4$ are solutions of integrals using Gauss-Legendre quadrature [19].

Power of volumetric heat source accumulated in the molten electrode material is expressed by formula [21]:

$$\dot{q}_v = \dot{m}(C_p(T_L - T_e) + L) \tag{14}$$

$$\dot{m} = \rho_e \frac{\pi d^2}{4} v_e \tag{15}$$

where: d is the diameter of the electrode, ρ_e is the density of the electrode material and v_e is wire feed speed, L is the heat of solidification [J/ kg], T_e - the initial value of the outputted from the welding head electrode, T_L – the temperature at which the molten metal drop separates from the electrode.

3. Phase transformation kinetics

Kinetics of phase transformations during heating is limited by temperature values at the beginning (A_1) and at the end (A_3) of austenitic transformation. The amount of austenite φ_A created during heating the ferrite-pearlitic steel is defined according to the Johnson-Mehl-Avrami's and Kolomogorov's (JMAK) rule [22]:

$$\varphi_A(T) = \sum_j \varphi_j^0\left(1 - exp\left(-b_j(T)t^{n_j(T)}\right)\right) \tag{16}$$

where φ_j^0 constitutes initial share of ferrite ($j \equiv F$), pearlite ($j \equiv P$) and bainite ($j \equiv B$), while constants b_j and n_j are determined using conditions of the beginning and the end of transformation:

$$n_j = \frac{ln(ln(0.99))}{ln(A_1 / A_3)} \tag{17}$$

$$b_j = \frac{0.01 n_i}{A_1} \tag{18}$$

In welding processes the volume fractions of particular phases during cooling depend on the temperature, cooling rate, and the share of austenite (in the zone of incomplete conversion $0 \leq \varphi_A \leq 1$). In quantitative perspective the progress of phase transformation during cooling is estimated using additivity rule by voluminal fraction φ_j of created phase what can be expressed analogically to Avrami's formula by equation [23]:

$$\varphi_j = \varphi_A \varphi_j^{max}\left(1 - exp\left(-b_j T^{n_j}\right)\right) + \varphi_j^0 \tag{19}$$

$$n_j = \frac{ln\left(ln\left(1 - \varphi_j^s\right) / ln\left(1 - \varphi_j^f\right)\right)}{ln\left(T_j^s / T_j^f\right)} \tag{20}$$

$$b_j = \frac{n_j\left(1 - \varphi_j^f\right)}{T_j^s} \tag{21}$$

$$\frac{\varphi_j^s}{\varphi_j^{max}} = 0.01 \ , \quad \frac{\varphi_j^f}{\varphi_j^{max}} = 0.99 \quad (22)$$

where: φ_j^0 is volume participation of j-th structural component, which has not been converted during the austenitization, $T_j^s = T_j^s(v_{8/5})$ and $T_j^f = T_j^f(v_{8/5})$ are respectively initial and final temperature of phase transformation of this component, , φ_j^{max} is the maximum volumetric fraction of phase j for the determined cooling rate estimated on the basis of the continuous cooling diagram (Fig. 5). while the integral volumetric fraction equals:
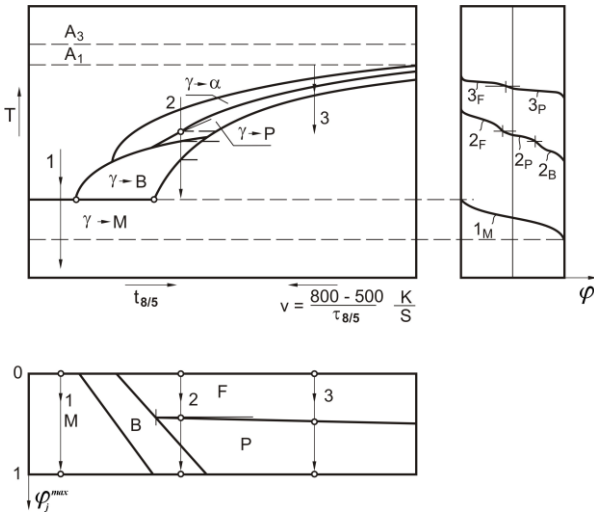
$$\sum_{j=1}^{k} \varphi_j = 1 \quad (23)$$

Figure 5. Scheme of phase changes of overcooled austenite depending on cooling velocity within temperature range 800-500 ^{0}C

The quantitative description of dependence of material's structure and quality on temperature and transformation time of over-cooled austenite during surfacing is made using the time-temperature-transformation diagram during continuous cooling, which binds the time of cooling $t_{8/5}$ (time when material stays within the range of temperature between 500 ^{0}C and 800 ^{0}C, or the velocity of cooling ($v_{8/5} = (800-500)/t_{8/5}$) and the temperature with the progress of phase transformation (Fig. 5). Those diagrams are called TTT–welding diagrams.

The fraction of martensite formed below the temperature M_s is calculated using the Koistinen-Marburger formula [24]:

$$\varphi_M(T) = \varphi_A \varphi_M^{max}\left\{1 - exp[-\mu(M_s - T)]\right\} \quad (24)$$

$$\mu = ln(\varphi_M^{min})/(M_s - M_f) \quad (25)$$

where φ_M denotes volumetric fraction of martensite, M_s and M_f denote initial and final temperature of martensite

transformation respectively, T the current temperature of process and $\varphi_M^{min} = 0.1$.

4. Thermal and structural strains

Total strain during single-pass surfacing represents the sum of thermal and structural strains during heating (ε^H) and cooling (ε^C):

$$\varepsilon(x,y,z,t) = \varepsilon^H + \varepsilon^C \quad (26)$$

Then strains during heating is equal to:

$$\begin{aligned}
\varepsilon^H = \sum_{i=A,P,F,B,M} &\left\{\alpha_i \varphi_{i0}(T - T_0)H(T_{A_1} - T) + \right.\\
&+ \alpha_i \varphi_i(T - T_{A_1})H(T_{A_3} - T)H(T - T_{A_1}) + \\
&\left. + \alpha_A(T - T_{A_3})H(T - T_{A_3}) + \varphi_i \gamma_{iA}\right\}
\end{aligned} \quad (27)$$

where: γ_{iA} – structural strain of i-th structure in austenite, T_0 – initial temperature, α_i - linear thermal expansion coefficient of i-th structure, and $H(x)$ is the function defined as follows:

$$H(x) = \begin{cases} 1 & for \ x > 0 \\ 0,5 & for \ x = 0 \\ 0 & for \ x < 0 \end{cases} \quad (28)$$

During cooling, the strain can be described by the relation:

$$\begin{aligned}
\varepsilon^C = &\ \alpha_A(T - T_{SOL})H(T - T_s) + \\
&+ \alpha_A(T_s - T_{SOL})H(T_s - T) + \\
&+ \sum_{i=A,P,F,B,M} \alpha_i \varphi_i(T - T_{si})H(T_{si} - T) + \\
&+ \sum_{i=P,F,B,M} \varphi_i \gamma_{Ai}
\end{aligned} \quad (29)$$

where T_{SOL} denotes solidus temperature, T_s – initial temperature of phase transformation, T_{si} - initial temperature of austenite transformation in i-th structure, γ_{Ai} – structural strain of austenite in i-th structure.
In addition, due to the limit on solid state of material:

$$\varepsilon(x,y,z,t) = 0 \quad for \ \ T > T_{SOL} \quad (30)$$

5. Model of stress calculation

Considered is longitudinally surfaced element, length of which is much bigger than its crosswise size. To describe stress state has been used prismatic rod subjected to mechanical strains, which for separate cross sections x are characterised by internal forces $N = N(x)$ and $M_y = M_y(x)$. Remaining forces are assumed to be negligible (transverse forces: $T_y = T_y(x)$, $T_z = T_z(x)$) and absent ($M_x = M_x(x)$). The

rod is also subjected to symmetric action in relation to z axis in slowly changing temperature field $T = T(x,y,z) = T(x,-y,z)$. This field is characterised by low temperature gradient in relation to the variable x. The stress state of the flat is characterised by single dimensional stress state $\sigma_x = \sigma_x(x,z,t) = \sigma_x(x,-y,z,t)$ (Fig. 6).
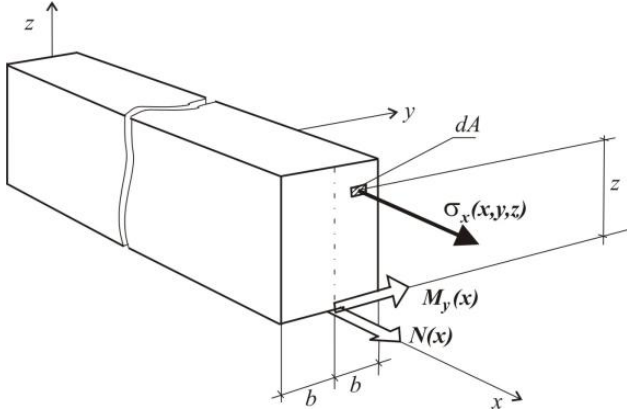

Figure 6. Scheme of rod subjected to mechanical and thermal loads

In order to derive formulas on strain and displacement of flat, Cauchy's relation has been used and planar section hypothesis has been assumed. In considered case, i.e. for technical theory of bent rods, differential equations of equilibrium are not used.

Instead, integral conditions of equilibrium using simple Hooke's law $\sigma_x = E\varepsilon_x$ are applied [25]. For modulus of longitudinal elasticity changeable towards coordinates (heterogeneous material of flat) or Young`s modulus dependent on temperature, stress can be described by:

$$\sigma = \frac{E}{A^E J_y^E - (S_y^E)^2}$$
$$\left\{ J_y^E \left(N(x) + N^T \right) + S_y^E \left(M(x) - M_y^T \right) + \right. \tag{31}$$
$$\left. - A^E \left(M(x) - M_y^T \right) + S_y^E \left(N(x) + N^T \right) z \right\}$$
$$- E\varepsilon_0 - \alpha E T$$

where:

$$A^E = \int\limits_{(A)} E dA \quad S_y^E = \int\limits_{(A)} Ez dA \quad J_y^E = \int\limits_{(A)} Ez^2 dA$$
$$N^T = \int\limits_{(A)} \alpha E T dA \quad M_y^T = \int\limits_{(A)} \alpha E T z dA \tag{32}$$

The stresses in elasto-plastic state are determined by iteration using method of elastic solutions at the variable modulus of longitudinal elasticity conditioned by the stress-strain curve [26]. Dependence of stresses on strains is assumed on the basis of tensile curves of particular structures, taking into account the influence of temperature.

6. Example of calculation

Calculations of the temporary temperature field for a square steel element with the side length 0,2 m and thickness of the plate 0,03 m made from steels S355J2G3 have been conducted. Thermal properties of welded subject material and electrode have been determined by $a = 8 \cdot 10^{-6}$ m^2/s, $C_p = 670$ J/kg K, $\rho = 7\,800$ kg/m^3 and $L = 268$ kJ/kg.

Numerical simulation has been conducted for the welding heat source of power 3 500 W, which corresponds to welding parameters ($U = 30$ V, $I = 400$ A, $\eta = 0,95$). In calculations there were assumed welding velocity $v = 0,007$ m/s, electrode wire diameter $d = 3,5$ mm, wire feed speed $v_e = 0,031$ m/s and bead dimensions $h_w = 2,5$ mm and $w_w = 22$ mm ($d_p = 0$). The initial value of temperature of electrode $T_e = 100$ °C (a temperature of contact tip with the welding head). Computations have been made for middle cross-section of the surfaced element.

In Figure 7 maximum temperature distribution in cross section has been presented. The calculated isotherm 1 493 °C determines the fusion line and isotherms A_3 and A_1 determine the partial and full austenitization zones (Fig. 8). In the Figure 3, the selected cross section points were marked, for which an stress analysis were performed. The temperatures $A_3 = 920$ °C and $A_1 = 748$ °C have been calculated taking into account the effect of heating rate on these temperatures [27]. The photograph of a metallographic macrosection in the middle cross section is shown in Figure 9. Calculated solidus isotherm 1 493 °C (solidification temperature of steel) - black line - corresponds to the fusion line obtained in the experiment. Bright line corresponds to the calculated temperature limit of the full transformation of austenite A_3.

The phase transformations kinetics during heating is limited by the temperatures A_1 of the beginning and A_3 the end of the austenite transformation, while the progress of phase transformations during cooling was determined on the basis of TTT-welding diagram for S355 steel shown in Fig. 10 [28].). The heat cycles and changes in phase shares at selected points of the cross section (comp. Fig. 8) are presented in Figs. 11 - 14. In all of the thermal cycles peaks illustrate maximum temperatures during weld beads.
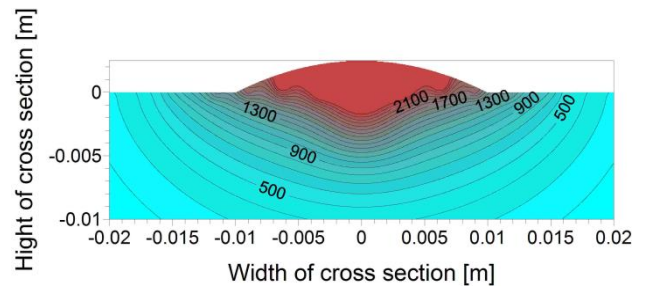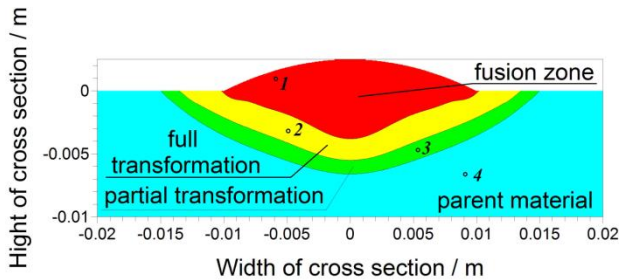

Figure 7. Maximum temperature field

Figure 8. Calculated heat affected zones

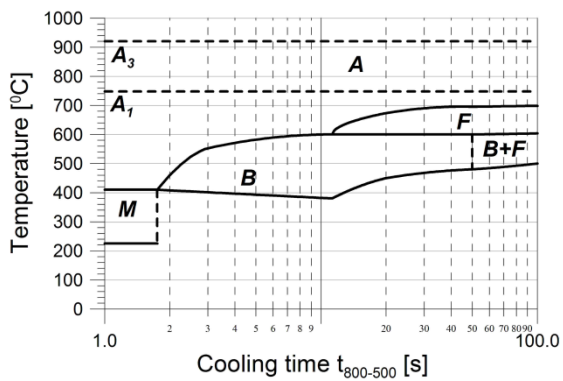**Figure 9.** Comparison of numerical results and image of metallographic section
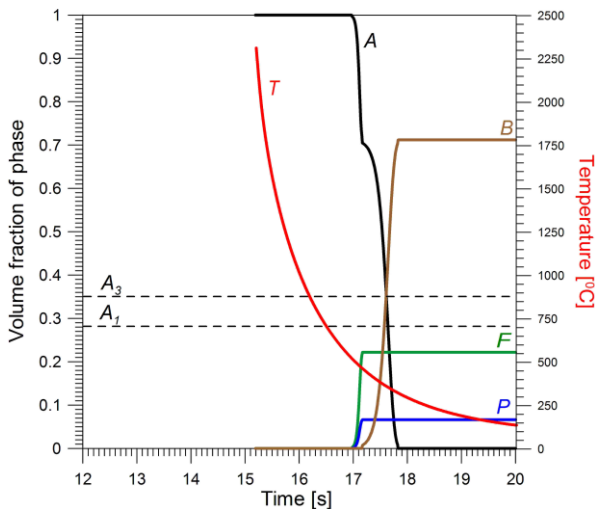

Figure 10. TTT-welding diagram for S355 steel

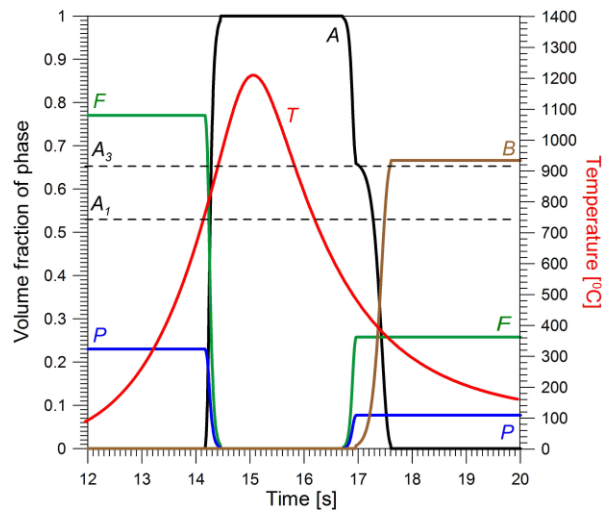**Figure 11.** Thermal welding cycle and phase shares at point *1*

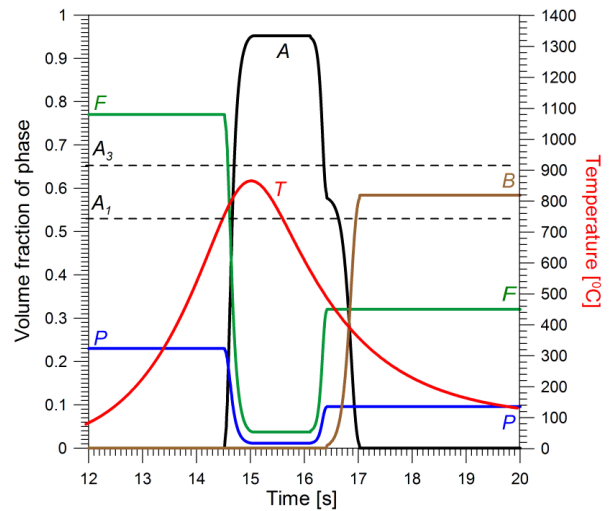**Figure 12.** Thermal welding cycle and phase shares at point *2*
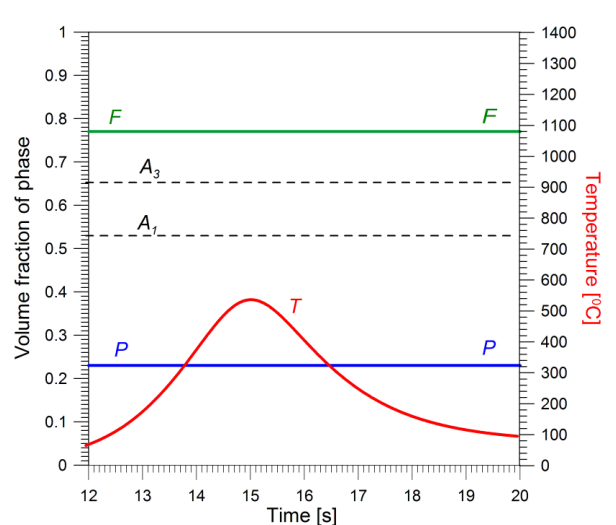

Figure 13. Thermal welding cycle and phase shares at point *3*

Figure 14. Thermal welding cycle and phase shares at point *4*

Table 1. Structural (γ) and thermal (α) expansion coefficients of phases [29]

	α [1/°C]		γ
Austenite	$2.178 \cdot 10^{-5}$	$\gamma_{F,P,S \to A}$	$1.986 \cdot 10^{-3}$
Ferrite	$1.534 \cdot 10^{-5}$	$\gamma_{B \to A}$	$1.440 \cdot 10^{-3}$
Pearlite	$1.534 \cdot 10^{-5}$	$\gamma_{A \to F,P}$	$3.055 \cdot 10^{-3}$
Bainite	$1.171 \cdot 10^{-5}$	$\gamma_{A \to B}$	$4.0 \cdot 10^{-3}$
Martensite	$1.36 \cdot 10^{-5}$		

In strain calculations there were assumed linear expansion coefficients of particular structural elements and structural stresses (Tab. 1) determined on the basis of the author's own dilatometric research [29].
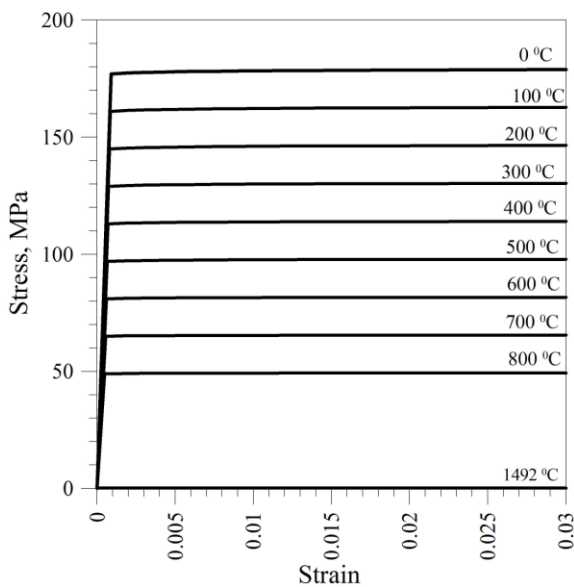

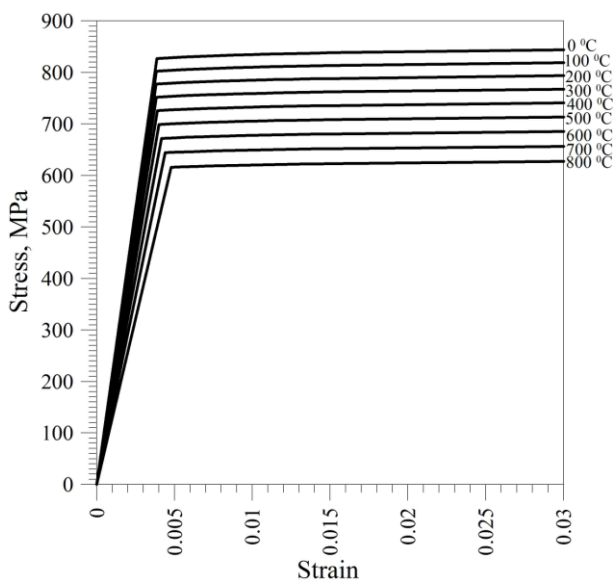**Figure 15.** Tensile curves of austenite
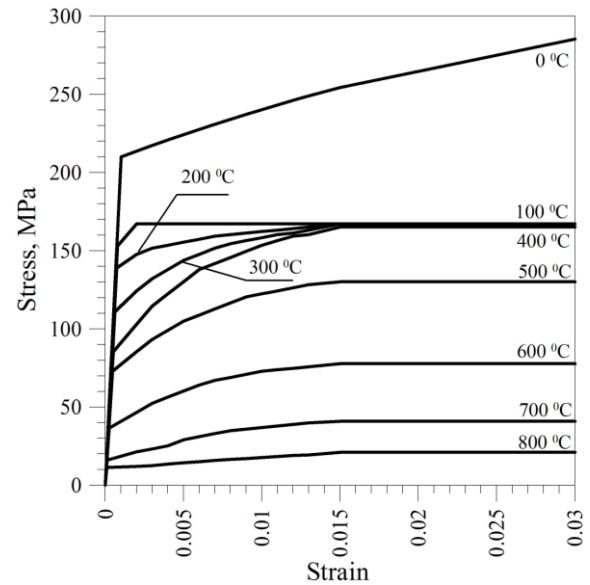

Figure 16. Tensile curves of bainite

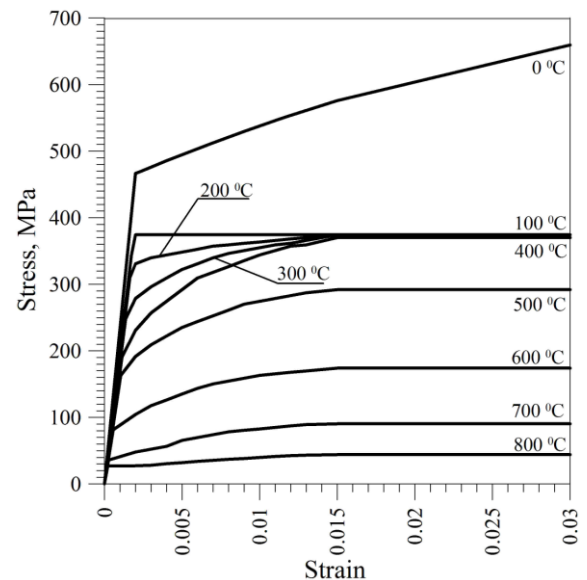**Figure 17.** Tensile curves of ferrite

Figure 18. Tensile curves of pearlite

Tensile curves of ferrite and pearlite are assumed on the basis of works [30, 31]. In case of austenite, bainite and martensite on the basis of data from works [32, 33] tensile curves are determined according to Swift law [34]. Tensile curve models of particular structures depending on temperature are presented in Figs. 15 –19.

Residual normal stresses distribution in the middle cross section at the distance between –0.02 m and 0.02 m from the weld axis has been presented in Fig. 20, while for the whole cross-section of the element has been presented in Fig. 21. Similar distributions of normal residual stresses were obtained in experimental studies conducted by Chang et al. [35] and with use of FEM by Jiang et al. [36].
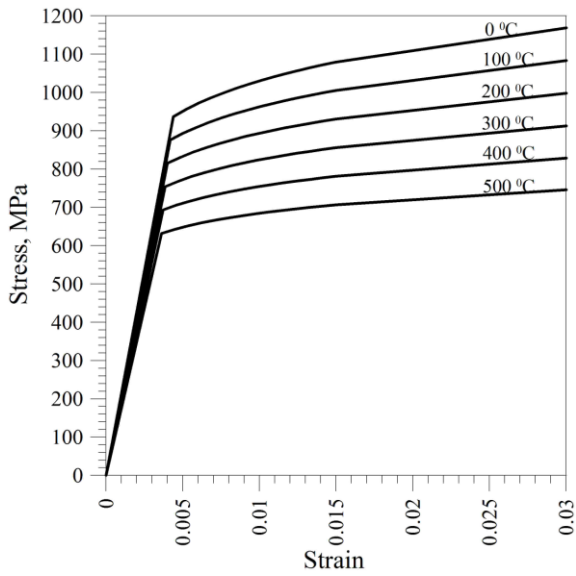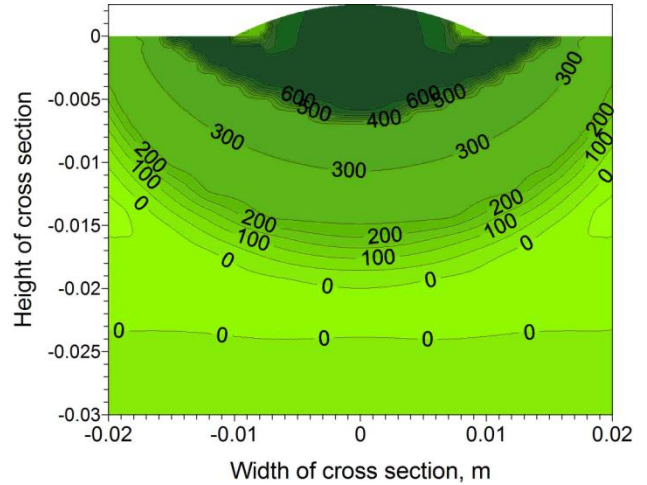
Figure 19. Tensile curves of martensite

Figure 20. Residual normal stresses in the middle part-area of cross section of plate
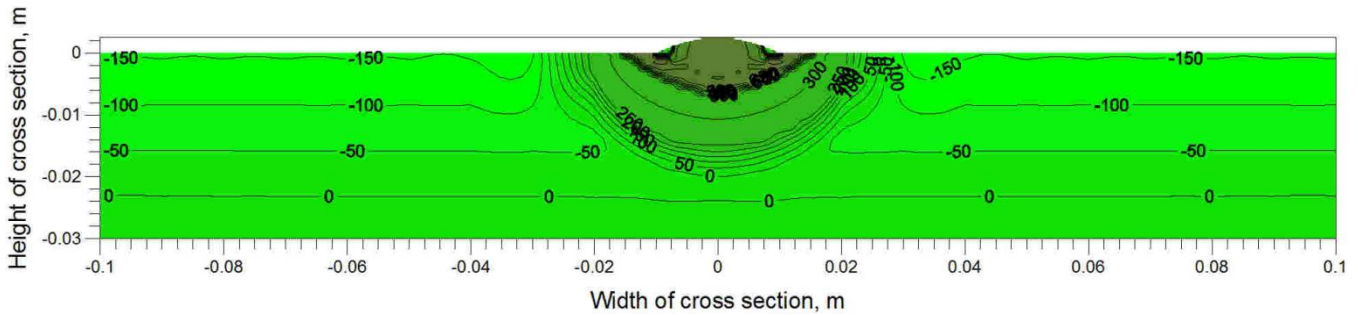

Figure 21. Residual normal stress distribution in the cross section of plate

In Figures 22 – 25 the history of stress states changes at selected points of cross section has been presented (see. Fig. 8). At point *1* from the weld area (Fig. 22), stresses amount to zero as long as the point is in a state of liquid metal. After solidification during cooling tensile stresses increase. Sudden transformation of stresses into compressive is caused by phase transformation. At point *2* (Fig. 23) from the area of full transformation due to the heating, the compressive stresses occur. Then, due to transformation of initial structure into austenite, stress state changes into tensile. Next, tensile stresses, being under the influence of further temperature growth, decrease but during cooling stresses increase again. During phase transformations of overcooled austenite into ferrite, pearlite and bainite stresses plunge becoming compressive. Then during further cooling compressive stresses decrease but values of tensile stresses increase. At point *3* (Fig. 24) from the area of partial transformation during heating compressive stresses increase, but then due to austenitization transform into tensile. During transformation the cooling begins, what causes further, much slower growth of tensile stresses. Transformations during cooling cause the decrease in values of tensile stresses and change of their sign.
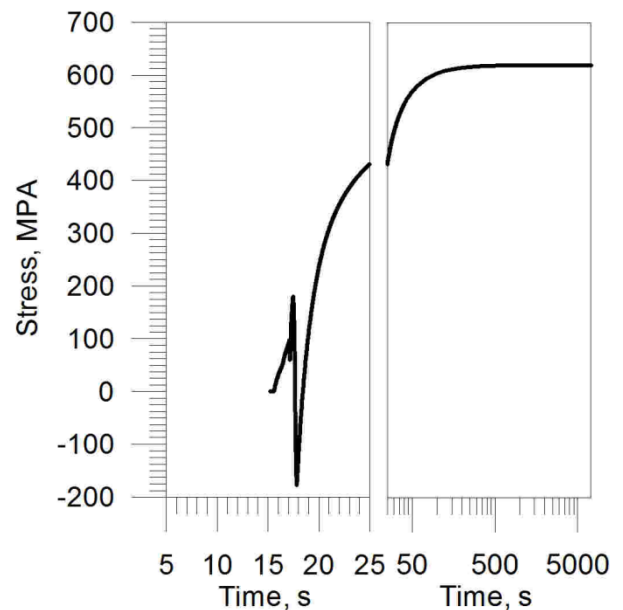

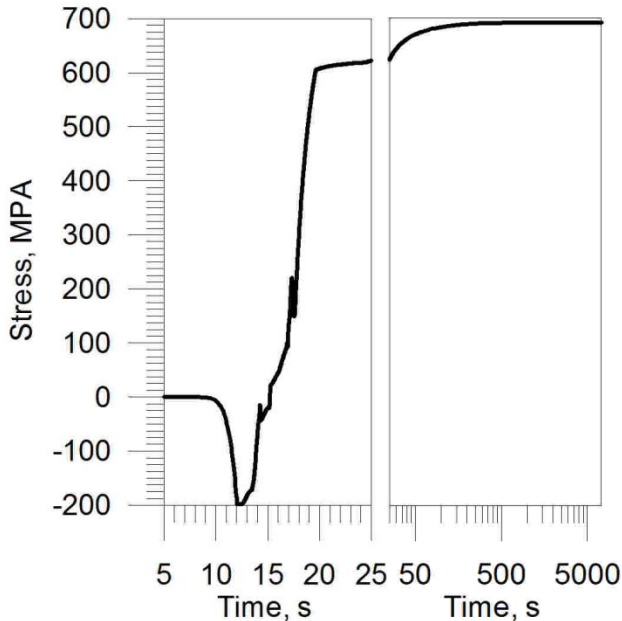**Figure 22.** Normal stresses at point *1* during surfacing
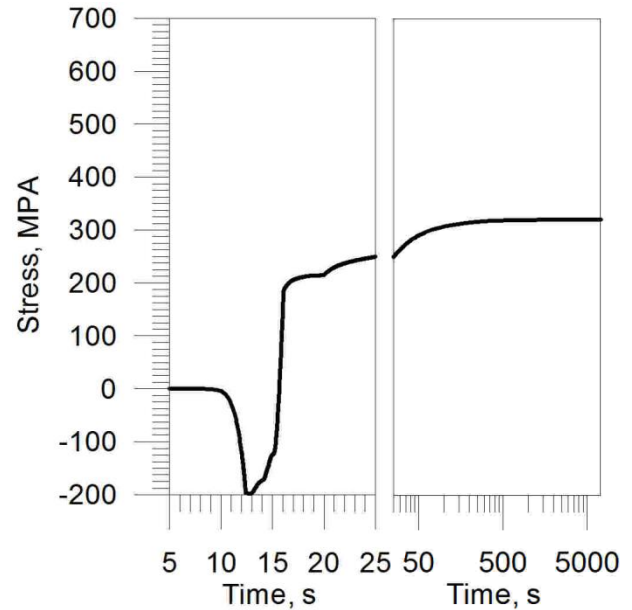
Figure 23. Normal stresses at point *2* during surfacing
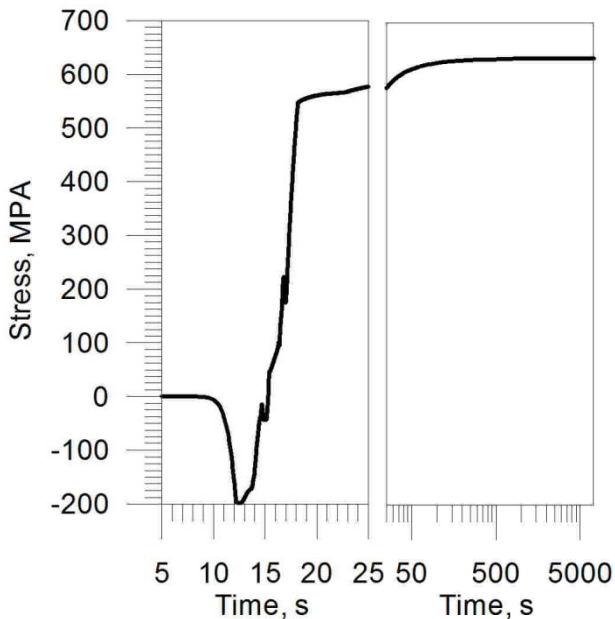

Figure 24. Normal stresses at point *3* during surfacing

Figure 25. Normal stresses at point *4* during surfacing

7. Conclusion

Presented model allows analysing and interpreting the influence of temperature field and phase transformations on strains and stresses caused by welding process using SAW method. Calculated temperature field, volume fractions of phases and stresses in longitudinally surfaced elements enable:

(i)   determination of heat affected zone, including areas of full and partial phase transformation as well fusion zone,

(ii)   analysis of stresses in any given point of section, investigation of phase volume fraction changes and strains and stresses caused by temperature changes and by phase transformations,

(iii)   analysis of stress states and plastic strain fields in rods during surfacing and residual stresses distribution after SAW surfacing.

Calculated state of residual stresses is characterised by high values of tensile stresses in weld, fusion and full transformation zones as well as by sudden decrease of their values in partial transformation zone. Correctness of such residual stress distribution was proved experimentally and in numerical simulations using FEM by other authors.

After phase transformations, due to further cooling, compressive stresses decrease, while tensile start to increase. At point *4* (Fig. 25) from the parent material area change of stress states results from temperature changes, changes of yield stress and from stress equilibrium in the cross-section. Compressive stresses increase during heating but decrease during cooling, becoming tensile stresses.

References

[1]   FACHINOTTI, V.D., ANCA, A.A., CARDONA, A. (2011) Analytical solutions of the thermal field induced by moving double-ellipsoidal and double elliptical heat sources in a semi-infinite body. *Int. J. Num. Meth. Biomech. Eng*. **27**: 595-607.

[2]   ANTONAKAKIS, T., MAGLIONI, C., VLACHOUDIS, V. (2013) Closed form solutions of the heat diffusion

equation with Gaussian source. *Int. J. Heat Mass Transf.* **62**: 314–322.

[3] GHOSH, A., BARMAN, N., CHATTOPADHYAYA, S., HLOCH, S. (2013) A study of thermal behaviour during submerged arc welding. *Strojniški vestnik – J. Mech. Eng.* **59**: 333-338.

[4] FRANKO, A., ROMOLI, L., MUSACCHIO, A. (2014) Modelling for predicting seam geometry in laser beam welding of stainless steel. *Int. J. Thermal. Sci.* **79**: 194-205.

[5] SALIMI, S., BAHEMMAT, P., HAGHPANAHI, M. (2014) A 3D transient analytical solution to the temperature field during dissimilar welding processes. *Int. J. Mechn. Sci.* **79**: 66-74.

[6] DAI, H-L., ZHENG Z-Q., XU W-L., LIU H-B., LUO A-H. (2017) Thermoviscoelastic dynamic response for a rectangular steel plate under laser processing, *Int. J. Heat Mass Transf.* **105**: 24-33.

[7] FENG S., HUANG C., WANG J., ZHU H., YAO P., LIU Z. (2017) An analytical model for the prediction of temperature distribution and evolution in hybrid laser-waterjey micro-machining. *Precision Eng.* **47**: 33-45.

[8] MAHAPATRA, M.M., DATTA, G.L., PRADHAN, B. (2006) Three-dimensional finite element analysis to predict the effects of shielded metal arc welding process parameters on temperature distributions and weldment zones in butt and one-sided fillet welds. *Proc. I. Mech. – J. Eng. Manuf.* **220**: 837-845.

[9] KUMAR, A., T. DEBROY, T. (2007) Heat transfer and fluid flow during gas-metal-arc fillet welding for various joint configurations and welding positions. *Metall. Mater. Trans.* **38A**: 506-519.

[10] WANG, S., GOLDAK, J., ZHOU, J., TCHERNOV, S., DOWEY, D. (2009) Simulation on the thermal cycle of a welding process by space-time convection-diffusion finite element analysis. *Int. J. Thermal. Sci.* **48**: 936-947.

[11] LEE, H.T., CHEN, C.T., WU, J.L. (2010) 3D numerical study of effects of temperature field on sensitisation of Alloy 690 butt welds fabricated by gas tungsten arc welding and laser beam welding. *Sci. Tech. Weld. Join.* **15**: 605-612.

[12] PIEKARSKA, W., KUBIAK, M. (2011) Three-dimensional model for numerical analysis of thermal phenomena in laser-arc hybrid welding process. *Int. J. Heat Mass Transf.* **54**: 4966-4974.

[13] CHEN, Y., HE, Y., CHEN, H., ZHANG, H., CHE, S. (2014) Effect of weave frequency and amplitude on temperature field in weaving welding process. *Int. J. Adv. Manuf. Techn.* **75**: 803–813.

[14] KONAR R., MICIAN M., PATEK M., KADAS D. (2016) Finite element modeling and numerical simulation of welding at the repair of gas pipelines with steel sleeve. *Manufacturig Technology* **16**: 360-365.

[15] MIKAMI Y., NAKAMURA T., MOCHIZUKI M. (2016) Numerical investigation of the influence of heat Skurce modeling on simulated residua stress distribution in weaving welds, *Weld. World* **60**:41-49.

[16] JIANG, Z., HUA, X., HUANG, L., WU, D., LI F., (2017) Effect of multiple thermal cycles on metallurgical and mechanical properties during multi-pass gas metal arc welding of Al 5083 alloy. *Int. J, Adv. Manuf. Technol.* **93**: 3799–3811.

[17] WINCZEK J., GAWROŃSKA E. (2016) The modeling of heat affected zone (HAZ) in submerged arc welding (SAW) surfacing steel element. *Metalurgija* **55**(2): 225 – 228.

[18] WINCZEK, J. (2010) Analytical solution to transient temperature field in a half-infinite body caused by moving volumetric heat source. *Int. J. Heat Mass Transf.* **53:** 5774-5781.

[19] WINCZEK, J. (2011) New approach to modeling of temperature field in surfaced steel elements. *Int. J. Heat Mass Transf.* **54**: 4702-4709.

[20] VISHNU, LI, W.B., EASTERLING, K.E. (1991) Heat-flow model for pulsed welding, *Mat. Sci. Tech.* **7:** 649-659.

[21] MODENESI, P.J., REIS, R.I. (2007) A model for melting rate phenomena in GMA welding, *J. Mater. Proccess. Tech.* **189:** 199-205.

[22] AVRAMI, M. (1939) Kinetics of phase change. I. General theory, *J. Chem. Phys.* **7**: 1103-1112.

[23] PIEKARSKA, W., KUBIAK, M., SATERNUS, Z. (2011) Numerical simulation of thermal phenomena and phase transformations in laser-arc hybrid welded joints, *Arch. Metall. Mater.* **56**: 409-421.

[24] DOMAŃSKI, T., BOKOTA A. (2011) Numerical models of hardening phenomena of tools steel base on the TTT and CCT diagrams, *Arch. Metal. Mater.* **56**: 325–344.

[25] WINCZEK, J. (2013) The analysis of stress states in steel rods surfaced by welding. *Archiv. Metal. Mater.* **58**: 1243–1252 (2013).

[26] BOKOTA, A., PARKITNY, R. (2003) Modelling of thermal, structural and mechanical phenomena in hardening processes of steel elements. In Piela A. [ed.] *Informatics in Metal Technology* (Gliwice: Silesian Univ. Technol.), ch. 7.

[27] PIEKARSKA, W., KUBIAK, M. (2012) Theoretical investigation into heat transfer in laser-welded steel sheets. *J. Therm. Anal. Calorim.* **10**: 159-166.

[28] BRÓZDA, J., PILARCZYK, J., ZEMAN, M. (1983) *TTT-welding diagrams transformation of austenite*, (Katowice: Śląsk).

[29] WINCZEK, J., KULAWIK, A. (2012) Dilatometric and hardness analysis of C45 steel tempering with different heating-up rates. *Metalurgija*, **51**(1): 9 – 12.

[30] GAWĄD, J., SZELIGA, D., BATOR, A., PIDVYSOCKYY, V., PIETRZYK, M. (2004) Interpretation of the tensile test results interpretation based on two criterion optimization, In: *Proc. 11. Conf. KomPlasTech, Informatics in Metal Technology*, Zakopane, 11–14.01.2004 (Kraków: Akapit), 27-34.

[31] VILA REAL, P.M.M., CAZELI, R., SIMOES DA SILVA, L., SANTIAGO, A., PILOTO, P. (2004) The effect of residual stresses in the lateral-torsional buckling of steel I-beams at elevated temperature. *J. Constr. Steel Res.* **60**: 783-793.

[32] MELANDER, M. (1985) *A computional and experimental investigation of induction and laser hardening* (Linkoping: Linkoping Univeristy).

[33] LIAN, J., JIANG, Z., LIU, J. (1991) Theoretical model for the tensile work hardening behaviour of dual-phase steel. *Mater. Sci. Eng.* **A147**: 55 – 65.

[34] KIM, S.K., KIM, Y.M., LIM, Y.J., KIM N.J. (2006) Relationship between yield ratio and the material constants of the swift equation. *Metals Materials Int.* **12**(2):131-135.

[35] CHANG P.H., TENG T.L. (2004) Numerical and experimental investigations on the residual stresses of the butt-welded joints. *Comput. Mater.Sci.* **29**: 511 –522.

[36] JIANG W., LIU Z., GONG J.M., TU S.T. (2010) Numerical simulation to study the effect of repair width on residual stresses of stainless steel clad plate, *Int. J. Pres. Ves. Pip.* **87**: 457 – 463.